
# Polymorphism in Non-Fullerene Acceptors Based on Indacenodithienothiophene

ADVANCED FUNCTIONAL MATERIALS
www.afm-journal.de

# Polymorphism in Non-Fullerene Acceptors Based on Indacenodithienothiophene

*Sara Marina, Alberto D. Scaccabarozzi, Edgar Gutierrez-Fernandez, Eduardo Solano, Aditi Khirbat, Laura Ciammaruchi, Amaia Iturrospe, Alex Balzer, Liyang Yu, Elena Gabirondo, Xavier Monnier, Haritz Sardon, Thomas D. Anthopoulos, Mario Caironi, Mariano Campoy-Quiles, Christian Müller, Daniele Cangialosi, Natalie Stingelin, and Jaime Martin**

**Organic solar cells incorporating non-fullerene acceptors (NFAs) have reached remarkable power conversion efficiencies of over 18%. Unlike fullerene derivatives, NFAs tend to crystallize from solutions, resulting in bulk heterojunctions that include a crystalline acceptor phase. This must be considered in any morphology-function models. Here, it is confirmed that high-performing solution-processed indacenodithienothiophene-based NFAs, i.e., ITIC and its derivatives ITIC-M, ITIC-2F, and ITIC-Th, exhibit at least two crystalline forms. In addition to highly ordered polymorphs that form at high temperatures, NFAs arrange into a low-temperature metastable phase that is readily promoted via solution processing and leads to the highest device efficiencies. Intriguingly, the low-temperature forms seem to feature a continuous network that favors charge transport despite of a poorly order along the $\pi$–$\pi$ stacking direction. As the optical absorption of the structurally more disordered low-temperature phase can surpass that of the more ordered polymorphs while displaying comparable—or even higher—charge transport properties, it is argued that such a packing structure is an important feature for reaching highest device efficiencies, thus, providing guidelines for future materials design and crystal engineering activities.**

## 1. Introduction

Organic solar cells (OSCs) have attracted great attention in the last 20 years as they promise cost-effective, clean, and renewable energy in addition to devices with complex form factors.[1] Most efficient OSCs include a blend of an electron-donating semiconducting polymer and an electron-accepting semiconducting small molecule arranged in a co-continuous phase-separated morphology known as bulk heterojunctions (BHJs).[2] Although fullerene derivatives have traditionally been the preferred choice for the realization of BHJs, so-called non-fullerene acceptors (NFAs) have recently emerged leading to significantly higher performances,[3] predominantly owing to a stronger absorption in the visible and near-IR (NIR) regions and the surprisingly long exciton diffusion length.[4]

S. Marina, Dr. E. Gutierrez-Fernandez, E. Gabirondo, Dr. H. Sardon, Dr. J. Martín
POLYMAT
University of the Basque Country
UPV/EHU Av. de Tolosa 72, San Sebastián 20018, Spain
E-mail: jaime.martin.perez@udc.es

Dr. A. D. Scaccabarozzi, Prof. T. D. Anthopoulos
King Abdullah University of Science and Technology (KAUST)
KAUST Solar Center (KSC)
Thuwal 23955, Saudi Arabia

The ORCID identification number(s) for the author(s) of this article can be found under https://doi.org/10.1002/adfm.202103784.



**DOI: 10.1002/adfm.202103784**

Dr. A. D. Scaccabarozzi, Dr. M. Caironi
Center for Nano Science and Technology@PoliMi
Istituto Italiano di Tecnologia
via Giovanni Pascoli 70/3, Milan 20133, Italy

Dr. E. Solano
ALBA Synchrotron Light Source
NCD-SWEET Beamline
Cerdanyola del Vallès 08290, Spain

A. Khirbat, A. Balzer, Prof. N. Stingelin
School of Materials Science and Engineering and School of Chemical & Biomolecular Engineering
Georgia Institute of Technology
311 Ferst Drive, Atlanta, GA 30332, USA

Dr. L. Ciammaruchi, Dr. M. Campoy-Quiles
Instituto de Ciencia de Materiales de Barcelona (ICMAB-CSIC)
Campus UAB, Bellaterra 08193, Spain

Dr. A. Iturrospe, Dr. X. Monnier, Dr. D. Cangialosi
Centro de Física de Materiales (CFM) (CSIC–UPV/EHU)
Materials Physics Center (MPC)
Paseo Manuel de Lardizabal 5, San Sebastián 20018, Spain

Dr. L. Yu, Prof. C. Müller
Department of Chemistry and Chemical Engineering
Chalmers University of Technology
Göteborg 41296, Sweden

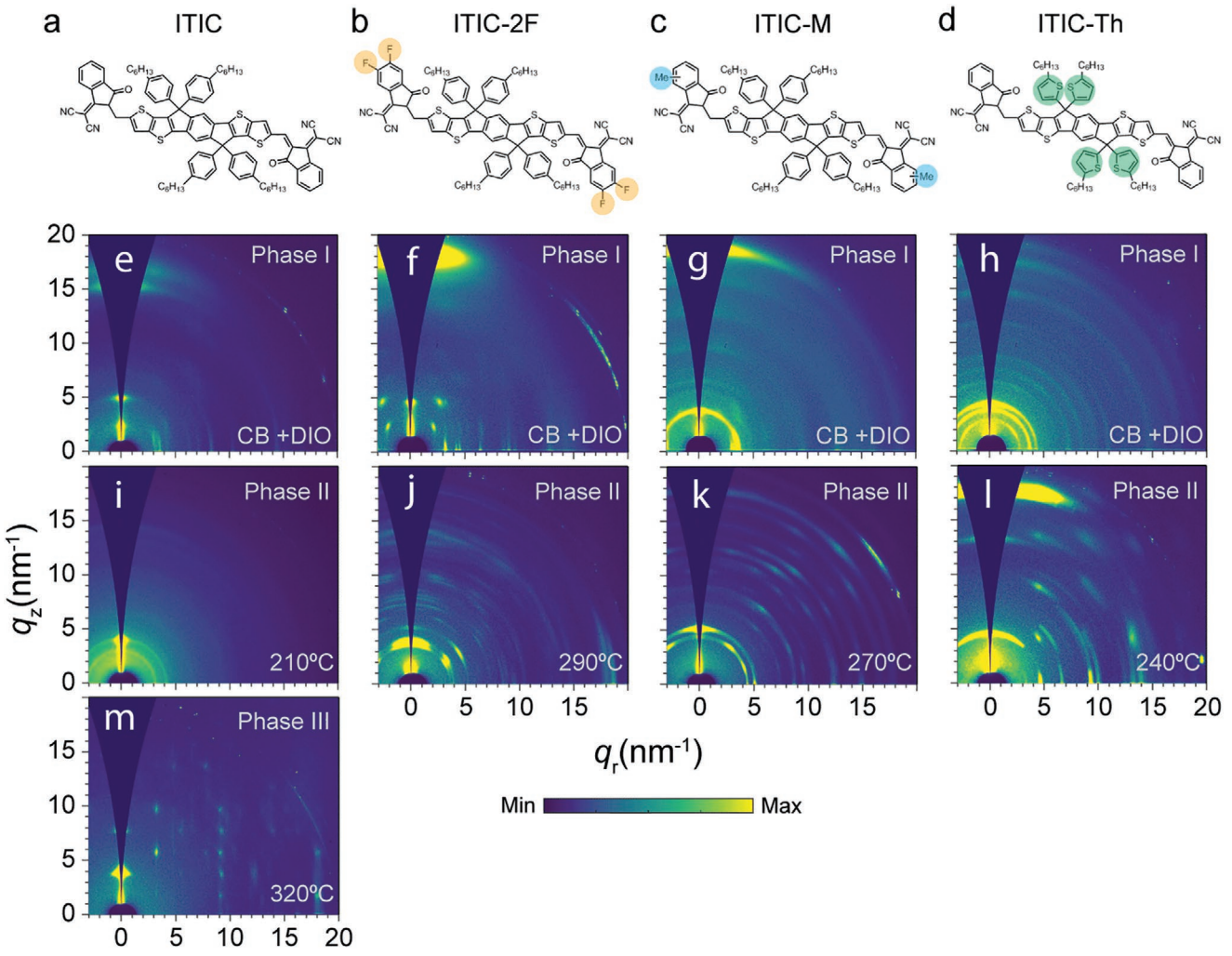


**Figure 1.** a–d) Chemical structures of ITIC, ITIC-2F, ITIC-M, and ITIC-Th, respectively. 2D GIWAXS patterns for ITIC e) Phase I, i) Phase II, and m) Phase III; ITIC-2F crystallized in f) Phase I and j) Phase II; ITIC-M crystallized in g) Phase I and k) Phase II; and ITIC-Th crystallized in h) Phase I and l) Phase II. All Phase I forms are produced by casting chlorobenzene (CB) solutions containing small amounts of DIO (0.5–1%). Phases II and III are obtained by annealing the thin films at the temperatures indicated in each panel.

Dr. X. Monnier
Donostia International Physics Center (DIPC)
Paseo Manuel de Lardizabal 4, San Sebastián 20018, Spain
Dr. D. Cangialosi
Centro de Fisica de Materiales (CSIC-UPV/EHU)
Paseo Manuel de Lardizabal 5, San Sebastián 20018, Spain
Prof. N. Stingelin
Laboratoire de Chimie des Polymères Organiques–LCPO
UMR5629 Universitéde Bordeaux
Allée Geoffroy Saint Hilaire
Bâtiment B8 CS50023, Pessac Cedex 33615, France
Dr. J. Martin
Universidade da Coruña
Grupo de Polímeros
Departamento de Física e Ciencias da Terra
Centro de Investigacións Tecnolóxicas (CIT)
Esteiro, Ferrol 15471, Spain
Dr. J. Martin
Ikerbasque
Basque Foundation for Science
Bilbao 48013, Spain

A highly successful example of a NFA is the indacenodithienothiophene-based molecule ITIC (chemical structure is shown in **Figure 1**a). Originally synthesized by Zhan and coworkers in 2015,[5] ITIC is an A-D-A structured molecule with indacenodithieno[3,2-*b*]thiophene (IT) as the central donor unit and with 2-(3-oxo-2,3-dihydroinden-1-ylidene)malononitrile (IC) as acceptor end groups. While ITIC delivered initially a relatively modest power conversion efficiency (PCE), optimization of device processing,[6] and incorporation of various chemical functionalities, such as fluorination (ITIC-2F, Figure 1b[7]), methylation (ITIC-M, Figure 1c[8]) or substitution of phenyl units by thiophene units (ITIC-Th, Figure 1d[9]), led to an increase of the PCE up to 14%.[10]

Unlike fullerene derivatives,[11] NFAs, including ITIC derivatives, often develop crystalline domains when they are solution-processed (e.g., by spin-coating or wire-bar coating).[12] As a result, the solid-state microstructure and phase morphology of polymer:NFA BHJs often include a crystalline acceptor phase, which must be considered in morphology/structure–function

models of such OSCs, especially as NFAs often can crystallize in various polymorphs, i.e., in different crystal forms.[13] Accordingly, it is of utmost importance to identify the structural, optical, and electronic characteristics of the various crystalline phases NFAs can feature. However, few studies have addressed the often-rich phase behavior of these promising acceptor materials. Hence, the impact of the different crystalline forms on the electronic properties still remains poorly understood.

Molecular polymorphism may affect device performance via different mechanisms: for example, different polymorphs can exhibit different optoelectronic properties because of different overlap between $\pi$-orbitals.[14] Moreover, crystal habits might differ between polymorphs, affecting the overall microstructure and leading to different BHJ phase morphologies.

The occurrence of polymorphism in organic materials, including organic semiconductors,[15] was originally rationalized in terms of the empirical Ostwald's rule of stages,[16] which states that in the crystallization of polymorphic systems, the most thermodynamically stable form is the last to appear. The polymorph initially formed is less thermodynamically stable but the activation energy required to overcome the barrier to form it is lower. In the case of solidification from solution, which is inherent to solution-processed organic semiconducting devices, this can be due to a favorable solvent-polymorph interfacial free energy.[15a]

Polymorphism might be closely connected to device efficiency of OSCs. Indeed, it has been recently reported that the slight increase in the degree of crystallinity of the ITIC domains in PBDB-T:ITIC BHJs, e.g., by thermal annealing below the glass transition temperature of ITIC ($T_g^{ITIC} \approx 180$ °C),[12c] by solvent annealing (with THF),[12b] or by the addition of solvent additives during the processing,[17] leads to the enhancement of both the device performance and device stability.[18] However, the increase in the degree of crystallinity achieved by annealing the devices at temperatures above the $T_g$ of ITIC was detrimental, drastically reducing the PCE.[12c] To rationalize the above results, Yu et al.[12c] and Ciammaruchi et al.[19] have suggested that ITIC is able to crystallize into different polymorphs, i.e., a low-temperature polymorph that develops via diffusion limited crystallization at temperatures below $T_g$ and a high-temperature polymorph that develops by regular cold crystallization at temperatures above the $T_g$.

In this paper, we identify, characterize, and gain understanding of the crystalline forms of indacenodithienothiophene-based NFAs, namely, ITIC, ITIC-M, ITIC-2F, and ITIC-Th. We make the following key observations: we find that all four NFAs exhibit polymorphism, including a low-temperature metastable polymorph that is characterized by continuous 1D-chain or multidimensional mesh-like aromatic structures and seemingly poor structural order along the $\pi$–$\pi$ stacking direction. As similar packing motifs have been reported for the best performing NFAs, including ITIC, IDTBR, and the benchmark Y6[13,20] (molecular structure Figure S1, Supporting Information) our work suggests that these crystal forms are a common feature for the highest-performing electron acceptors for OSCs. We, thus, provide a rationale for future materials discovery. Indeed, our study reveals that these phases can exhibit higher optical absorption than the higher ordered, high-temperature polymorphs, and display comparable—or even higher—charge transport properties with respect to the latter.

## 2. Results and Discussion

We begin our discussion by identifying the different polymorphic phases in solution processed (spin-cast) indacenodithienothiophene-based NFAs. Unless otherwise stated, the analyzed samples were 90 to 110-nm-thick films processed by spin-coating 20 mg mL$^{-1}$ solutions at 2000 rpm, which are standard processing conditions in OSC device manufacturing[7,21] (see profilometry data in Figure S2, Supporting Information). We find that all spin-cast indacenodithienothiophene-based NFAs exhibit polymorphism: three different polymorphs are found in case of ITIC, denoted as Phase I, Phase II, and Phase III, while ITIC-M, ITIC-2F, and ITIC-Th exhibit two polymorphs, namely, Phase I and Phase II. Low-temperature Phase I polymorphs develop in NFAs during casting under specific processing conditions (discussed in detail later) while Phase II polymorphs (and Phase III in ITIC) are obtained upon thermal treatment. Grazing incidence wide angle X-ray scattering (GIWAXS) patterns of all crystal forms found in indacenodithienothiophene-based NFAs are shown in Figure 1e–m and Figures S4 and S5 (Supporting Information). **Table 1** summarizes the position and the crystal coherence length (CCL), calculated using the Scherrer equation[22] of the main diffraction peaks.

In agreement with previous literature on NFAs packing motifs, the GIWAXS patterns for low-temperature Phase I forms of ITIC, ITIC-M, ITIC-2F, and ITIC-Th are identified by multiple intense diffraction peaks in the low-$q$ region and few

**Table 1.** Peak position and crystalline coherence length (CCL) values of the GIWAXS reflections for identified ITIC-X polymorphs when annealing the material ex situ at the relevant temperatures followed by cooling to ambient temperature at 50 °C min$^{-1}$. * CCL was calculated with the Scherrer equation: CCL $= 2 \cdot \pi \cdot k/\Delta q$ ($k = 0.9$) and $\Delta q$ as the full width at half maximum of the given peak.

| NFA | Polymorphs | Periodic aromatic-aliphatic packing | | $\pi$–$\pi$ peak | |
|---|---|---|---|---|---|
| | | $q$ [nm$^{-1}$] | CCL [nm] | $q$ [nm$^{-1}$] | CCL [nm] |
| ITIC | Phase I | 3.2 | 23.2 | 15.5 | 4.0 |
| | | 3.6 | 23.8 | 17.1 | 5.1 |
| | | 4.7 | 14.7 | | |
| | | 5.1 | 11.3 | | |
| | Phase II | 3.2 | 24.0 | – | – |
| | | 4.1 | 18.1 | | |
| | Phase III | 4.1 | 11.7 | 18.1 | 5.9 |
| ITIC-2F | Phase I | 2.5 | 64.9 | 18.1 | 3.5 |
| | | 3.2 | 29.7 | | |
| | | 4.2 | 24.4 | | |
| | | 4.6 | 16.1 | | |
| | Phase II | 3.7 | 37.2 | 18.5 | 16.7 |
| | | 4.1 | 23.4 | | |
| ITIC-M | Phase I | 3.0 | 36.5 | 18.6 | 5.8 |
| | | 3.8 | 15.5 | | |
| | Phase II | 4.4 | 23.4 | 18.0 | 6.6 |
| | | 5.3 | 15.7 | | |
| ITIC-Th | Phase I | 2.8 | 20.2 | 17.3 | 7.2 |
| | | 3.8 | 18.8 | | |
| | | 4.4 | 18.2 | | |
| | Phase II | 4.7 | 16.1 | 17.9 | 7.4 |

peaks in the high-$q$ region. To gain information about lattice characteristics and for peak indexing, the GIWAXS patterns were fitted with GIWAXS-SIIRkit[23] (details are included in Figure S6 and Table S1, Supporting Information). We note that our attempts to perform single-crystal diffraction of Phase I crystals failed, which prevented us from conducting a more refined analysis of packing motifs.

The GIWAXS patterns found suggest packing motifs where NFA molecules pack into 1D-chain or multidimensional mesh-like structures, as those proposed previously for NFA single crystals,[12d,13a,b,20,24] which are expected to exhibit a high magnitude of electron transfer integral and therefore efficient charge transfer between molecules. Because 1D- or mesh-like packing motifs feature continuous aromatic structures that are separated by aliphatic domains,[13,20] many large $d$-spacing symmetry planes exist, which are expected to give rise to multiple diffraction peaks in the low-$q$ region, as found in our patterns.[20d] This conjecture is further supported by our observation that the main aromatic–aliphatic periodicity peaks and the $\pi$–$\pi$ stacking—the signature of which are the intense diffraction peaks showing up at high-$q$ values—point both along the same direction (i.e., the out-of-plane direction), at least for low-temperature phases in ITIC, ITIC-M, and ITIC-2F. Having aliphatic groups in ITIC-based NFAs pendant from the central building blocks, terminal acceptor groups are free to $\pi$–$\pi$ stack with further terminal groups promoting continuous aromatic structures that result in 1D- or multidimensional structures.

Low-temperature Phase I polymorphs are promoted in films cast from aromatic solvents like chlorobenzene (CB), 1,2-orthodichlorobenzene ($o$-DCB), or 1,2-orthoxylene ($o$-Xy). This can be deduced from the data obtained for both spin and drop-cast films (Figures S7–S10, Supporting Information, respectively). We note that the ITIC-Th Phase I can also be produced from dichloromethane (DCM) solutions. Nonetheless, ITIC-Th behaves slightly different from the rest of NFAs. Moreover, we find that Phase I is favored if a small amount of 1,8-diiodooctane (DIO), an additive frequently used during processing of OSCs, is added to the casting solution (Figures S11 and S12, Supporting Information).[6,7,10] This behavior is most probably associated to the low vapor pressure of the DIO that allows more extensive NFA crystallization to occur prior to the vitrification of noncrystallized regions, i.e., DIO remains in the almost solidified film and acts as a plasticizer.[25]

High-temperature polymorphs, i.e., Phase II (for ITIC-M and ITIC-2F) and Phase III (for ITIC) exhibit, in general, a higher amount of well-defined diffraction peaks compared to Phase I forms, which highlights that the former lattices exhibit more symmetry elements and, likely, larger ordered domains than their Phase I counterparts. Phases II and III result when NFAs are thermally treated. For example, ITIC Phase III develops at temperatures above 270 °C from Phase I and at 220 °C from amorphous ITIC (Figure 1m and Figures S13 and S14, Supporting Information). ITIC Phase II polymorph is obtained by heating Phase I at intermediate temperatures between Phase I and Phase III (Figure 1i). Interestingly, the stability region for Phase II seems to be dependent on the film thickness, which would agree with a thermotropic behavior that is dependent on spatial confinement (Figures S13 and S14, Supporting Information).[26] Finally, Phase II polymorphs develop during heating ITIC-M, ITIC-2F, and ITIC-Th films at, respectively, 220, 220, and 170 °C (Figures S15 and S16, Supporting Information).

Dominant interactions between organic semiconducting molecules, including the ITIC derivatives studied here, are in general weak, e.g., van der Waals, $\pi$–$\pi$ interactions, hydrogen bonds, and/or electrostatic interactions, which, in addition, are frequently nonspecific. This results in the general tendency of organic semiconductors to adopt multiple packing modifications upon solidification.[15a] Moreover, the main chemical difference between these NFAs—at least ITIC, ITIC-M, and ITIC-2F—results from their terminal acceptor groups that can lead to intermolecular interactions. Hence, the differences in the physicochemical characteristics of terminal groups (e.g., electronegativity, volume), resulting from the different chemical functionality, might alter the intermolecular packing and, eventually, the development of a diverse polymorph set.

Interestingly, the phase behavior of ITIC-Th seems to differ from that of the other NFAs (as already alluded to above), possibly because the different chemical moiety in ITIC-Th is in the central building block and not in the terminal groups. More specifically, unlike the low-temperature Phase I of ITIC, ITIC-M, and ITIC-2F, the GIWAXS patterns for ITIC-Th Phase I do not exhibit an intense and broad $\pi$–$\pi$ peak. This observation agrees with the packing motif reported for $\beta$-ITIC-Th single crystals.[13a] The high-temperature Phase II, however, shows a clearer $\pi$–$\pi$ stacking signal, which is likely related to the $\alpha$-ITIC-Th lattice reported in ref. [20b]. Moreover, our patterns for ITIC-Th Phase I and Phase II are similar to those reported in ref. [12d], where such a Phase I pattern was interpreted as resulting from co-crystallization of ITIC and ITIC-Th into chain-like packing structures. Even if the formation of chain-packing structures seems possible, our data suggest that the patterns correspond to two different ITIC-Th polymorphs.

To gain understanding of the polymorphism of indacenodithienothiophene-based NFAs from a thermodynamic viewpoint, temperature-resolved in situ GIWAXS and differential scanning calorimetry (DSC) experiments were conducted (heating rate was 10 and 20 °C min$^{-1}$, respectively). Here, we will base our discussion on the data obtained for ITIC, which is shown in **Figure 2**, while the corresponding results for the remaining derivatives are included in Figure S15 (Supporting Information) (it should be stressed, however, that ITIC exhibits one more polymorph than the other derivatives). We must note here again that ITIC-Th seems to exhibit a different thermotropic behavior compared to the rest of NFAs. We argue, using an energy diagram depicted in Figure 2d, that Phase I polymorphs (of ITIC, OTIC-M, and ITIC-2F) are thermodynamically metastable whereas high-temperature Phase II and Phase III are thermodynamically stable phases. We base our hypothesis that Phase I forms are metastable on the following main arguments: i) Phase I melts before evolving into Phase II. Clear indications of the above are the loss of birefringence (Figure 2a), the loss of Bragg diffractions at about 180 °C (Figure 2b), and the presence of an endothermic peak in DSC in the same temperature region (Figure 2c). ii) Phase I is not formed during cooling. We deduce this from the POM data in Figures S17–S20 (Supporting Information) and the GIWAXS data given in, e.g., Figure 1, which displays the patterns of Phases II and III acquired from

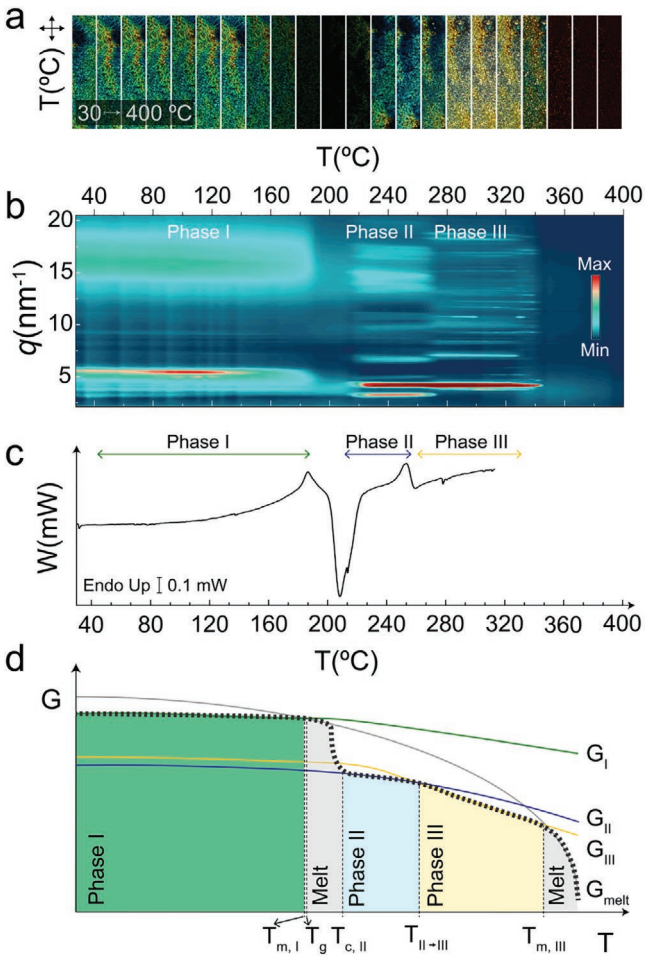


**Figure 2.** a) Polarized optical microscopy (POM) images of a drop-cast ITIC thin film acquired during a heating ramp from 30 to 400 °C at 10 °C $min^{-1}$ under $N_2$ flow (the acquisition temperatures, *T*, are indicated in the images). The size of the images in the horizontal direction corresponds to 100 µm. b) Contour plot of the azimuthal integrations 2D GIWAXS patterns (from a 20 mg $mL^{-1}$ chlorobenzene solution) acquired from room temperature up to 400 °C at 10 °C $min^{-1}$ recorded for a drop-cast ITIC film. c) DSC first heating scan (from a 10 mg $mL^{-1}$ chlorobenzene solution) acquired during a heating ramp from −50 to 320 °C at 20 °C $min^{-1}$. d) Schematic free energy (*G*) versus temperature (*T*) diagram for ITIC crystalline phases. The green, blue, yellow, and gray solid lines correspond to the free energy for Phases I, II, III and the ITIC melt ($G_m$), respectively. The dashed red line describes the evolution of *G* for a 100% crystalline ITIC during heating. $T_{m,I}$, $T_{c,II}$, $T_{II\rightarrow III}$, and $T_{m,III}$ represent the phase transition temperatures from Phase I to molten ITIC, from Phase II to Phase III and from Phase III to ITIC melt, respectively.

samples that were first thermally annealed (for 5 min) at the temperatures indicated and then cooled to 25 °C at 50 °C $min^{-1}$. As for ITIC-Th, or data shown in Figures S15 and S16 (Supporting Information) evidence that contrarily to the rest of Phase I forms, ITIC-Th Phase I melts at similar temperatures as Phase II (i.e., 240–260 °C). Thus, once Phase I is achieved from solution casting, ITIC-Th does not transform into Phase II. Phase II just grows by cold crystallization from molten ITIC-Th at temperatures above $T_g$.

Being thermodynamically metastable, the Phase I crystal form of ITIC, ITIC-M, and ITIC-2F, which is the predominant phase reported in many devices,[12c,d] is expected to evolve with time into the thermodynamically stable phase, i.e., Phase II, which can compromise the long-term stability of the OSC devices. However, this seems not to occur during the lifetime of the devices. Indeed, a film stored for two years (in ambient conditions) still was solely comprised of the Phase I crystals (results included in Figure S21, Supporting Information). Indeed, while we did not observe changes in film structure when storing samples at ambient conditions for over two years, we cannot exclude that during device operation and exposure to sunlight (and, thus, heat), Phase I may gradually transform in either Phase II or III.

As tellingly, Phase II is a thermodynamically stable form, because i) it develops directly from the melt at about 210 °C and ii) the polymorphic transition between Phase II and Phase III seems to be enantiotropic, which means that Phase II and Phase III are both thermodynamically stable in their respective temperature ranges. We argue the above based on the fact that the transition is recorded as an endothermic peak during heating (Figure 2c) and the transition is reversible, i.e., the reverse transition from Phase III to Phase II is detected during cooling (Figures S22 and S23, Supporting Information). Phase III, however, would correspond to the thermodynamically preferred crystalline Phase in ITIC because, it is the last form to evolve prior to the solid-melt transition, and it develops independently of the processing conditions applied (Figures S4, S13, and S14, Supporting Information).

Having rationalized the polymorphic behavior of ITIC-based NFAs, we went on to investigate the optoelectronic properties of the different polymorphs to gain insights why polymorph I phases generally lead to the highest-performing devices, as illustrated with devices comprising PBDB-T:ITIC and PBDB-T:ITIC-2F blends in the low-temperature Phase I and high-temperature polymorphs (these data are included in Figure S24, Supporting Information). We first focused on the charge transport properties of the different polymorphs, hypothesizing that different molecular packing may affect the latter. For this purpose, we fabricated organic field-effect transistors (OFETs), using a top-gate bottom-contact device architecture, as shown in **Figure 3**a. Representative transfer characteristics curves for ITIC Phase III, both in the linear ($V_d$ = 10 V) and saturation ($V_d$ = 60 V) regimes, from which the mobility values were extracted, are shown in Figure 3b, while the electrical characteristics of devices comprising the other polymorphs and molecules are included in Figures S25–S27 (Supporting Information). All the devices display similar electrical characteristics, hence the different polymorphs in the four derivatives investigated exhibit comparable saturation field-effect mobilities ($\mu_{sat}$), despite the seemingly inherent disorder along the $\pi$–$\pi$ stacking planes found in Phase I polymorphs (Figure 3a and Figure S25, Supporting Information, and **Table 2**), which may be expected to limit charge transport. More precisely, Phase II and Phase III ITIC devices show a slight enhancement of the mobility compared to Phase I devices, but the opposite trend is observed for ITIC-M, ITIC-2F, and ITIC-Th, for which higher saturation mobility values are measured for Phase I than for Phase II. We argue that despite the disorder of the $\pi$-stack, the continuous aromatic structures in Phase I polymorphs facilitate long-range charge transport.

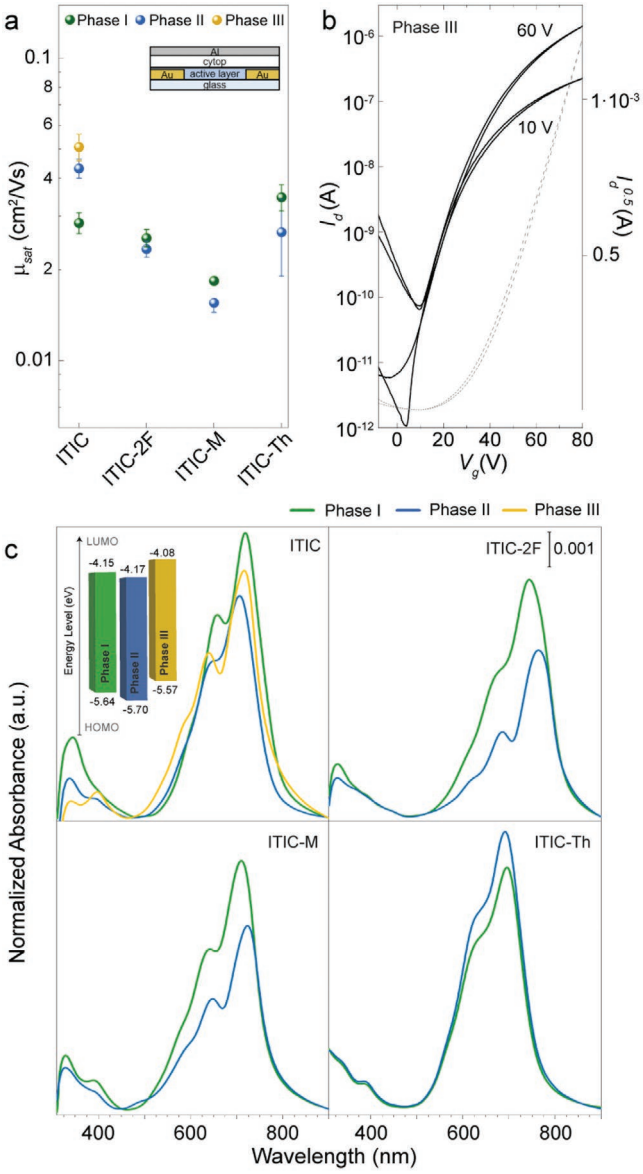


**Figure 3.** a) Saturation field-effect mobility, $\mu_{sat}$, values measured for the different ITIC polymorphs. The inset shows a schematic of the OFET device architecture used. b) Representative transfer characteristic of ITIC Phase III (annealed at 270 °C for 5 min) in the linear ($V_d$ = 10 V) and saturation ($V_d$ = 60 V) regimes. Dashed line corresponds to the square root of the current in saturation regime. c) Room temperature UV–vis absorption spectra for Phase I (green lines), Phase II (blue lines), and Phase III (yellow lines) for ITIC, ITIC-2F, ITIC-M, and ITIC-Th. The inset in the upper left panel shows the energetic levels for the three ITIC polymorphs found, as calculated from ultraviolet photoelectron spectroscopy (UPS) and UV–vis data.

Intriguingly, strong differences in the optical absorption and emission of the NFA films crystallized in Phase I, Phase II, and Phase III were found in UV–vis absorption and photoluminescence spectroscopy (PL) measurements (Figure 3c and Figure S28, Supporting Information, respectively). UV–vis absorption and PL measurements for each NFA were performed at room temperature on a single sample crystallized into Phase I and Phase II (and Phase III in the ITIC case), so that absorbed intensities for the different polymorphs are comparable (absorption and PL data are furthermore normalized to the thickness of each film). Our data clearly show that the light absorption (and emission) is significantly stronger in Phase I polymorphs than the high-temperature polymorphs, i.e., Phase II in ITIC-2F, ITIC-M, and ITIC-Th and Phase II and III in ITIC. This is interpreted to result from an increased J-aggregate coupling in continuous aromatic structures found in Phase I forms. This could favor the performance of Phase I compared to the other forms (Phases II and III) in photovoltaic devices (device data are included in Figure S24, Supporting Information). However, we must also note that the higher performance of devices containing Phase I may in addition originate from a more suitable donor:acceptor blend nanomorphology, i.e., a shorter phase separation length scale, as probed by GISAXS (Figure S29, Supporting Information).

A further analysis of the absorption spectra reveals that the absorption maxima ($\lambda_{max}$) of the high-temperature polymorphs (Phases II and III) appear, in general, to be slightly redshifted compared to that of Phase I polymorphs. This results in lower optical bandgaps ($E_g$) for the former phases (data are summarized in Table 2). Phase II of ITIC is the exception (solid blue line in Figure 3c) as it exhibits a $\lambda_{max}$ and an absorption onset that is blueshifted, resulting in a larger optical bandgap ($E_g$).

The energetic levels of the ITIC polymorphs were assessed in more detail using ultraviolet photoelectron spectroscopy (UPS) (details are included in Figure S31, Supporting Information). As shown in the inset of the upper panel in Figure 3c, the HOMO level of Phase I is at 5.64 eV, that of Phase II is at 5.70, and the one for Phase III is at 5.57 eV. The LUMO levels, on the other hand, are at 4.15, 4.17, and 4.08 eV for Phase I, Phase II, and Phase III, respectively. Therefore, in principle, while differences exist, all polymorphs in ITIC exhibit relatively good energy level aligment relative to the donor polymers from the benzodithiophene-benzodithiophenedione-based donor copolymer family, such as PBDB-T[12b] (molecular structure in Figure S1, Supporting Information), thus, being an unlikely cause for Phase I being better performing than Phases II and III.

## 3. Conclusions

In summary, our work establishes that high-performing indacenodithienothiophene-based NFAs exhibit at least two crystalline phases: a low-temperature metastable polymorph that is characterized by continuous 1D-chain or multidimensional mesh-like, continuous aromatic structures and seemingly poor structural order along the $\pi$–$\pi$ stacking direction, and a highly ordered thermodynamically stable high-temperature phase (or phases, in the case of ITIC). Interestingly, packing motifs as found for the low-temperature polymorphs (continuous aromatic structures, poor $\pi$–$\pi$ stacking) seem to be a common feature among best performing OSCs, including ITIC, IDTBR, and the benchmark Y6,[13,20] probably resulting from a chemical structure with aliphatic chains pendant from the central molecular building blocks while the terminal acceptor groups are free to $\pi$–$\pi$ stack into a continuous network. The excellent device performance of Phase I polymorphs is assigned to the fact that such structures exhibit a stronger light absorption than

**Table 2.** Relevant temperatures and optoelectronic parameters for the different microstructures identified in ITIC, ITIC-M, ITIC-2F, and ITIC-Th. Optical bandgap ($E_g$, estimated from $E_g\,(\text{eV}) = h{\cdot}\upsilon \approx 1240/\lambda_{a.e.}(\text{nm})$), maximum absorption wavelength ($\lambda_{max}$), saturation field-effect mobility ($\mu_{sat}$), Planck's constant ($h$), absorption edge values ($\lambda_{a.e.}$), and frequency ($\upsilon$).

| | ITIC | | | ITIC-2F | | ITIC-M | | ITIC-Th | |
|---|---|---|---|---|---|---|---|---|---|
| | Ph I | Ph II | Ph III | Ph I | Ph II | Ph I | Ph II | Ph I | Ph II |
| $\mu_{sat}$ [$cm^2\ V^{-1}\ s^{-1}$] | 0.028 | 0.043 | 0.05 | 0.025 | 0.023 | 0.018 | 0.016 | 0.034 | 0.027 |
| $E_g$ [eV] | 1.49 | 1.53 | 1.49 | 1.48 | 1.40 | 1.57 | 1.55 | 1.55 | 1.54 |
| $\lambda_{max}$ [nm] | 712 | 705 | 716 | 726 | 732 | 743 | 777 | 695 | 700 |

the high-temperature polymorphs (likely owing to an increased J-aggregate coupling), while they display comparable—or even higher—charge transport properties with respect to the latter polymorphs, likely resulting from an increased electron transfer integral. Clearly, a fair comparison between the OPV performance between low temperature Phase I and high-temperature phases is challenging to make because of the larger-scale phase separation that often accompanies the solid–solid phase transition from Phase I to Phases II and III polymorphs, which has a strong negative effect on device performance. Nonetheless, our results provide relevant and, likely, broadly applicable crystal engineering- and materials design guidelines. They also demonstrate that understanding of low-temperature Phase I polymorphs is critical to establish meaningful structure–function relationships for OSCs and to obtain insights, for instance, into the structural degradation mechanisms of NFA-based devices.

## 4. Experimental Section

*Materials*: The non-fullerene acceptor ITIC and the derivatives ITIC-M, ITIC-Th, and ITIC- 2F were supplied by Ossila Ltd. CB, *o*-DCB, chloroform ($CHCl_3$), dichloromethane ($CH_2Cl_2$), *o*-Xy, and DIO were purchased from Merck and used as received.

*Sample Preparation*: Solutions were spin-cast onto the substrate from a 20 mg $mL^{-1}$ concentration in the specified solvent at a spin rate of 2000 rpm during 60 s. For thick films, samples were directly drop-cast. The thermal treatments were performed as specified. The silicon substrates were positioned in a preheated hot stage (Linkam Scientific Instruments Ltd.) and annealed for 5 min. After heating, samples were cooled down at 50 °C $min^{-1}$ to room temperature. The edges of the samples were removed to eliminate edge effects in the GIWAXS experiment. i) ITIC Phase I: CB + 1% DIO; Phase II: CB + annealing at 210 °C for 5 min, and Phase III: CB + annealing at 320 °C for 5 min. ii) ITIC-2F Phase I: CB + 0.5% DIO; and Phase II: CB + annealing at 290 °C for 5 min. iii) ITIC-M Phase I: CB + 0.5% DIO; and Phase II: CB + annealing at 270 °C for 5 min. iv) ITIC-Th Phase I: CB + 0.5% DIO; and Phase II: CB + annealing at 240 °C for 5 min.

*Grazing Incidence Wide Angle X-Ray Scattering*: GIWAXS measurements were performed at the BL11 NCD-SWEET beamline at ALBA Synchrotron Radiation Facility (Spain). The incident X-ray beam energy was set to 12.4 eV using a channel cut Si (1 1 1) monochromator. The angle of incidence $\alpha_i$ was set between 0.1 and 0.15 to ensure surface sensitivity. The scattering patterns were recorded using a Rayonix LX255-HS area detector, which consists of a pixel array of 1920 × 5760 pixels ($H \times V$) with a pixel size of 44 × 44 $\mu m^2$. Data are expressed as a function of the scattering vector ($q$), which was calibrated using $Cr_2O_3$ as standard sample, obtaining a sample-to-detector distance of 145.6 mm. Temperature-resolved in situ X-ray experiments were performed using a Linkam THMS 600 stage adapted for grazing incidence experiments. The heating rate used was 10 °C $min^{-1}$ and the temperature difference between frames was 4 °C. Exposure times for in situ and ex situ experiments were 1 and 5 s, respectively. All the measurements were performed under $N_2$ atmosphere to minimize the damage of the films. 2D GIWAXS patterns were corrected as a function of the components of the scattering vector. Samples for GIWAXS were prepared by spin-casting 20 mg $mL^{-1}$ solutions on Si wafers at a spin rate of 2000 rpm. For thick film samples, the same solutions were directly drop-casted. The thermal treatments were performed in a Linkam hot stage under $N_2$ atmosphere. Edges of the samples were removed to eliminate edge effects in the GIWAXS experiment.

*Differential Scanning Calorimetry*: DSC was conducted under nitrogen at a scan rate of 20 °C $min^{-1}$ with a Mettler Toledo STARe System DSC 3+ instrument.

*UV–vis Absorption Spectroscopy*: UV–vis spectra were recorded with a Shimadzu UV-2550 spectrometer with a film adapter.

*Photoluminescence*: Photoluminescence spectra were recorded on a LS55 Perkin-Elmer Fluorescence spectrometer on the same samples analyzed by UV–vis.

*Ultraviolet Photoelectron Spectroscopy*: UPS was performed on a Kratos Axis Ultra XPS/UPS System using helium arc source with incident photon energy of 21.2 eV, a scan step size of 0.05 eV, and a dwell time of 200 ms from 25 to −5 eV. The workfunction was calculated by linearly fitting the high binding energy cutoff to the intercept, which is subtracted from the incident energy, 21.2 eV. The energy from the Fermi edge to the HOMO level was calculated by linearly fitting the low binding energy cutoff to the intercept.

*Field-Effect Transistor Fabrication and Measurement*: A standard top-gate bottom-contact configuration was used in the fabrication of field-effect transistors. Gold source/drain contacts were thermally evaporated on a borofloat glass after cleaning via ultrasonication in acetone and isopropanol and a subsequent $O_2$ plasma exposition at 100 W for 5 min. Solutions of the organic semiconductor were dissolved in chlorobenzene (10 mg $mL^{-1}$), stirred at 80 °C for 2 h and then spin-coated in a nitrogen-filled glovebox at 2000 rpm for 60 s. A Cytop layer (≈550–600 nm) was spin-coated on top of the semiconductor film at 4000 rpm, 400 rpm $s^{-1}$ for 90 s, and then an annealing at 90 °C was performed for 1 h. Al gate contact was finally thermally evaporated through a shadow mask. The devices were then tested in glovebox using a Keysight B2912A Precision Source/Measure Unit without exposing them to ambient conditions.

## Supporting Information

Supporting Information is available from the Wiley Online Library or from the author.

## Acknowledgements

This work was supported by the Ministerio de Ciencia e Innovacion/FEDER (under Ref. PGC2018-094620-A-I00 and PGC2018-095411-B-I00, CEX2019-000917-S, and PGC2018-095411-B-100) and the Basque Country Government (Ref. PIBA19-0051). S.M. is grateful to POLYMAT for the doctoral scholarship. The authors thank A. Arbe, A. Alonso-Mateo, and L. Hueso for their support and access to characterization tools.

The authors also thank the technical and human support provided by SGIker of UPV/EHU and European funding (ERDF and ESF). GIWAXS experiments were performed at BL11 NCD-SWEET beamline at ALBA Synchrotron (Spain) with the collaboration of ALBA staff. J.M and E.F.-G. acknowledge support through the European Union's Horizon 2020 research and innovation program, H2020-FETOPEN 01-2018-2020 (FET-Open Challenging Current Thinking), "LION-HEARTED," Grant Agreement No. 828984. J.M and N.S. would like to thank the financial support provided by the IONBIKE RISE project, which received funding from the European Union's Horizon 2020 research and innovation programme under the Marie Skłodowska-Curie Grant Agreement No. 823989. N.S., A.K., and A.B. furthermore are grateful to the U.S. National Science Foundation (NSF) for support via Project No. 1905901 within NSF's Division of Materials Research. A.S. and M.C. acknowledge financial support by the European Research Council (ERC) under the European Union's Horizon 2020 research and innovation program "HEROIC," Grant Agreement No. 638059. This work was partially carried out at Polifab, the micro- and nanotechnology center of the Politecnico di Milano. C.M. thanks the Knut and Alice Wallenberg Foundation for funding through the project "Mastering Morphology for Solution-borne Electronics." A.I. thanks MICINN for a Personal Técnico de Apoyo contract (PTA2017-14359-I) and gratefully acknowledge the financial support of the Basque Government (Research Groups IT-1175-19) and the MICINN (PGC2018-094548-B-I00, MCIU/AEI/FEDER, UE.

Funding for open access charge: Universidade da Coruña/CISUG.

## Conflict of Interest

The authors declare no conflict of interest.

## Data Availability Statement

Research data are not shared.

## Keywords

non-fullerene acceptors, organic electronics, organic semiconductors, organic solar cells, polimorphism

Received: April 21, 2021
Published online: May 13, 2021

[1] N. S. Sariciftci, L. Smilowitz, A. J. Heeger, F. Wudl, *Science* **1992**, *258*, 1474.

[2] J. J. M. Halls, C. A. Walsh, N. C. Greenham, E. A. Marseglia, R. H. Friend, S. C. Moratti, A. B. Holmes, *Nature* **1995**, *376*, 498.

[3] Y. Firdaus, V. M. Le Corre, J. I. Khan, Z. Kan, F. Laquai, P. M. Beaujuge, T. D. Anthopoulos, *Adv. Sci.* **2019**, *6*, 1802028.

[4] a) C. Yan, S. Barlow, Z. Wang, H. Yan, A. K. Y. Jen, S. R. Marder, X. Zhan, *Nat. Rev. Mater.* **2018**, *3*, 18003; b) Y. Lin, M. I. Nugraha, Y. Firdaus, A. D. Scaccabarozzi, F. Aniés, A.-H. Emwas, E. Yengel, X. Zheng, J. Liu, W. Wahyudi, E. Yarali, H. Faber, O. M. Bakr, L. Tsetseris, M. Heeney, T. D. Anthopoulos, *ACS Energy Lett.* **2020**, *5*, 3663; c) Y. Lin, Y. Firdaus, F. H. Isikgor, M. I. Nugraha, E. Yengel, G. T. Harrison, R. Hallani, A. El-Labban, H. Faber, C. Ma, X. Zheng, A. Subbiah, C. T. Howells, O. M. Bakr, I. McCulloch, S. D. Wolf, L. Tsetseris, T. D. Anthopoulos, *ACS Energy Lett.* **2020**, *5*, 2935; d) Y. Firdaus, V. M. Le Corre, S. Karuthedath, W. Liu, A. Markina, W. Huang, S. Chattopadhyay, M. M. Nahid, M. I. Nugraha, Y. Lin, A. Seitkhan, A. Basu, W. Zhang, I. McCulloch, H. Ade, J. Labram, F. Laquai, D. Andrienko, L. J. A. Koster, T. D. Anthopoulos, *Nat. Commun.* **2020**, *11*, 5220.

[5] Y. Lin, J. Wang, Z.-G. Zhang, H. Bai, Y. Li, D. Zhu, X. Zhan, *Adv. Mater.* **2015**, *27*, 1170.

[6] W. Zhao, D. Qian, S. Zhang, S. Li, O. Inganäs, F. Gao, J. Hou, *Adv. Mater.* **2016**, *28*, 4734.

[7] W. Zhao, S. Li, H. Yao, S. Zhang, Y. Zhang, B. Yang, J. Hou, *J. Am. Chem. Soc.* **2017**, *139*, 7148.

[8] S. Li, L. Ye, W. Zhao, S. Zhang, S. Mukherjee, H. Ade, J. Hou, *Adv. Mater.* **2016**, *28*, 9423.

[9] Y. Lin, F. Zhao, Q. He, L. Huo, Y. Wu, T. C. Parker, W. Ma, Y. Sun, C. Wang, D. Zhu, A. J. Heeger, S. R. Marder, X. Zhan, *J. Am. Chem. Soc.* **2016**, *138*, 4955.

[10] S. Zhang, Y. Qin, J. Zhu, J. Hou, *Adv. Mater.* **2018**, *30*, 1800868.

[11] P. Westacott, N. D. Treat, J. Martin, J. H. Bannock, J. C. de Mello, M. Chabinyc, A. B. Sieval, J. J. Michels, N. Stingelin, *J. Mater. Chem. A* **2017**, *5*, 2689.

[12] a) T. J. Aldrich, M. Matta, W. Zhu, S. M. Swick, C. L. Stern, G. C. Schatz, A. Facchetti, F. S. Melkonyan, T. J. Marks, *J. Am. Chem. Soc.* **2019**, *141*, 3274; b) Q. Liang, J. Han, C. Song, X. Yu, D.-M. Smilgies, K. Zhao, J. Liu, Y. Han, *J. Mater. Chem. A* **2018**, *6*, 15610; c) L. Yu, D. Qian, S. Marina, F. A. A. Nugroho, A. Sharma, S. Hultmark, A. I. Hofmann, R. Kroon, J. Benduhn, D.-M. Smilgies, K. Vandewal, M. R. Andersson, C. Langhammer, J. Martín, F. Gao, C. Müller, *ACS Appl. Mater. Interfaces* **2019**, *11*, 21766; d) J. Mai, Y. Xiao, G. Zhou, J. Wang, J. Zhu, N. Zhao, X. Zhan, X. Lu, *Adv. Mater.* **2018**, *30*, 1802888.

[13] a) S. Halaby, M. W. Martynowycz, Z. Zhu, S. Tretiak, A. Zhugayevych, T. Gonen, M. Seifrid, *Chem. Mater.* **2021**, *33*, 966; b) H. Lai, H. Chen, J. Zhou, J. Qu, M. Wang, W. Xie, Z. Xie, F. He, *J. Phys. Chem. Lett.* **2019**, *10*, 4737; c) S. M. Swick, T. Gebraad, L. Jones, B. Fu, T. J. Aldrich, K. L. Kohlstedt, G. C. Schatz, A. Facchetti, T. J. Marks, *ChemPhysChem* **2019**, *20*, 2608.

[14] a) G. Giri, S. Park, M. Vosgueritchian, M. M. Shulaker, Z. Bao, *Adv. Mater.* **2014**, *26*, 487; b) G. Giri, E. Verploegen, S. C. B. Mannsfeld, S. Atahan-Evrenk, D. H. Kim, S. Y. Lee, H. A. Becerril, A. Aspuru-Guzik, M. F. Toney, Z. Bao, *Nature* **2011**, *480*, 504; c) D. W. Davies, S. K. Park, P. Kafle, H. Chung, D. Yuan, J. W. Strzalka, S. C. B. Mannsfeld, S. G. Wang, Y.-S. Chen, D. L. Gray, X. Zhu, Y. Diao, *Chem. Mater.* **2021**.

[15] a) H. Chung, Y. Diao, *J. Mater. Chem. C* **2016**, *4*, 3915; b) H. Chung, S. Chen, N. Sengar, D. W. Davies, G. Garbay, Y. H. Geerts, P. Clancy, Y. Diao, *Chem. Mater.* **2019**, *31*, 9115; c) H. Chung, S. Chen, B. Patel, G. Garbay, Y. H. Geerts, Y. Diao, *Cryst. Growth Des.* **2020**, *20*, 1646; d) Y. Diao, K. M. Lenn, W.-Y. Lee, M. A. Blood-Forsythe, J. Xu, Y. Mao, Y. Kim, J. A. Reinspach, S. Park, A. Aspuru-Guzik, G. Xue, P. Clancy, Z. Bao, S. C. B. Mannsfeld, *J. Am. Chem. Soc.* **2014**, *136*, 17046; e) G. E. Purdum, N. Yao, A. Woll, T. Gessner, R. T. Weitz, Y.-L. Loo, *Adv. Funct. Mater.* **2016**, *26*, 2357; f) A. M. Hiszpanski, C. J. Dsilva, I. G. Kevrekidis, Y.-L. Loo, *Chem. Mater.* **2018**, *30*, 3330; g) G. E. Purdum, N. G. Telesz, K. Jarolimek, S. M. Ryno, T. Gessner, N. C. Davy, A. J. Petty, Y. Zhen, Y. Shu, A. Facchetti, G. E. Collis, W. Hu, C. Wu, J. E. Anthony, R. T. Weitz, C. Risko, Y.-L. Loo, *J. Am. Chem. Soc.* **2018**, *140*, 7519; h) G. Giri, R. Li, D.-M. Smilgies, E. Q. Li, Y. Diao, K. M. Lenn, M. Chiu, D. W. Lin, R. Allen, J. Reinspach, S. C. B. Mannsfeld, S. T. Thoroddsen, P. Clancy, Z. Bao, A. Amassian, *Nat. Commun.* **2014**, *5*, 3573; i) J. Chen, M. Shao, K. Xiao, A. J. Rondinone, Y.-L. Loo, P. R. C. Kent, B. G. Sumpter, D. Li, J. K. Keum, P. J. Diemer, J. E. Anthony, O. D. Jurchescu, J. Huang, *Nanoscale* **2014**, *6*, 449; j) L. Yu, N. Stingelin, *J. Org. Semicond.* **2013**, *1*, 16.

[16] W. Ostwald, *Z. Phys. Chem.* **1897**, *22*, 289.

[17] H. Chen, J. Qu, L. Liu, W. Chen, F. He, *J. Phys. Chem. Lett.* **2019**, *10*, 936.

[18] a) X. Du, T. Heumueller, W. Gruber, O. Almora, A. Classen, J. Qu, F. He, T. Unruh, N. Li, C. J. Brabec, *Adv. Mater.* **2020**,

*32*, 1908305; b) L. Ciammaruchi, O. Zapata-Arteaga, E. Gutiérrez-Fernández, J. Martin, M. Campoy-Quiles, *Mater. Adv.* **2020**, *1*, 2846.

[19] L. Ciammaruchi, O. Zapata-Arteaga, E. Gutiérrez-Fernández, J. Martin, M. Campoy-Quiles, *Mater. Adv.* **2020**, *1*, 2846.

[20] a) L. Zhu, M. Zhang, G. Zhou, T. Hao, J. Xu, J. Wang, C. Qiu, N. Prine, J. Ali, W. Feng, X. Gu, Z. Ma, Z. Tang, H. Zhu, L. Ying, Y. Zhang, F. Liu, *Adv. Energy Mater.* **2020**, *10*, 1904234; b) H. Bristow, K. J. Thorley, A. J. P. White, A. Wadsworth, M. Babics, Z. Hamid, W. Zhang, A. F. Paterson, J. Kosco, J. Panidi, T. D. Anthopoulos, I. McCulloch, *Adv. Electron. Mater.* **2019**, *5*, 1900344; c) H. Lai, H. Chen, J. Zhou, J. Qu, P. Chao, T. Liu, X. Chang, N. Zheng, Z. Xie, F. He, *iScience* **2019**, *17*, 302; d) D. Yan, W. Liu, J. Yao, C. Zhan, *Adv. Energy Mater.* **2018**, *8*, 1800204.

[21] L. Gao, Z.-G. Zhang, H. Bin, L. Xue, Y. Yang, C. Wang, F. Liu, T. P. Russell, Y. Li, *Adv. Mater.* **2016**, *28*, 8288.

[22] A. L. Patterson, *Phys. Rev.* **1939**, *56*, 978.

[23] V. A. Savikhin, H.-G. A. Steinruck, R.-Z. A. Liang, B. A. A. Collins, S. D. A. Oosterhout, P. M. A. Beaujuge, M. F. A. Toney, *J. Appl. Crystallogr.* **2020**, *53*, 1108.

[24] J. Qu, H. Chen, J. Zhou, H. Lai, T. Liu, P. Chao, D. Li, Z. Xie, F. He, Y. Ma, *ACS Appl. Mater. Interfaces* **2018**, *10*, 39992.

[25] a) M. T. Fontana, H. Kang, P. Y. Yee, Z. Fan, S. A. Hawks, L. T. Schelhas, S. Subramaniyan, Y.-J. Hwang, S. A. Jenekhe, S. H. Tolbert, B. J. Schwartz, *J. Phys. Chem. C* **2018**, *122*, 16574; b) Y. Zhang, A. J. Parnell, F. Pontecchiani, J. F. K. Cooper, R. L. Thompson, R. A. L. Jones, S. M. King, D. G. Lidzey, G. Bernardo, *Sci. Rep.* **2017**, *7*, 44269.

[26] J. Martín, M. Dyson, O. G. Reid, R. Li, A. Nogales, D.-M. Smilgies, C. Silva, G. Rumbles, A. Amassian, N. Stingelin, *Adv. Electron. Mater.* **2018**, *4*, 1700308.